npj | quantum materials

Article

Published in partnership with Nanjing University

https://doi.org/10.1038/s41535-024-00665-z

Multiferroic quantum material $Ba_2Cu_{1-x}Mn_xGe_2O_7$ ($0 \le x \le 1$) as a potential candidate for frustrated Heisenberg antiferromagnet

Henrik Thoma[1,2] ✉, Rajesh Dutta[1,2,10] ✉, Vladimir Hutanu[1,2] ✉, Veronica Granata[3], Rosalba Fittipaldi[4], Qiang Zhang[5], Jeffrey W. Lynn[6], Petr Čermák[7], Nazir Khan[8], Shibabrata Nandi[9] & Manuel Angst[9]

Multiferroic $Ba_2CuGe_2O_7$ was anticipated as a potential member of the exciting group of materials hosting a skyrmion or vortex lattice because of its profound Dzyaloshinskii–Moriya interaction (DMI) and the absence of single ion anisotropy (SIA). This phase, however, could not be evidenced and instead, it exhibits a complex incommensurate antiferromagnetic (AFM) cycloidal structure. Its sister compound $Ba_2MnGe_2O_7$, in contrast, is characterized by a relatively strong in-plane exchange interaction that competes with a non-vanishing SIA and the weak DMI, resulting in a quasi-two-dimensional commensurate AFM structure. Considering this versatility in the magnetic interactions, a mixed solid solution of Cu and Mn in $Ba_2Cu_{1-x}Mn_xGe_2O_7$ can hold an interesting playground for its interactive DMI and SIA depending on the mixed spin states of the transition metal ions towards the skyrmion physics. Here, we present a detailed study of the micro- and macroscopic spin structure of the $Ba_2Cu_{1-x}Mn_xGe_2O_7$ solid solution series using high-resolution neutron powder diffraction techniques. We have developed a remarkably rich magnetic phase diagram as a function of the applied magnetic field and x, which consists of two end-line phases separated by a potentially quantum-critical phase at $x = 0.57$. An AFM conical structure at zero magnetic field is demonstrated to persist up to $x = 0.50$. Our results provide crucial information on the spin structure and magnetic properties, which are necessary for the general understanding and theoretical developments on multiferroicity in the frame of skyrmion type or frustrated AFM lattice where DMI and SIA play an important role.

Melilite-type non-centrosymmetric multiferroic germanates $Ba_2TGe_2O_7$ (T = Cu, Mn, Co) are well known for exhibiting an unconventional metal-ligand d–p hybridization mechanism responsible for the spin-driven ferroelectricity[1,2]. Remarkable magnetoelectric physical properties and magnetic structures were comprehensively studied in refs. 1,3–8. These materials could offer a basis for device applications, utilizing their large induced electric polarization even under zero magnetic field. In general, strongly correlated electron systems including square lattice Heisenberg antiferromagnets with $S \ge \frac{1}{2}$ serve as an exciting reservoir for studying many exotic quantum phenomena[9–11]. Recent observations of intriguing physical phenomena in quasi-two-dimensional (2D) $Ba_2CoGe_2O_7$ and related compounds, like unconventional spin excitations, formation of complex

[1]Institut für Kristallographie, RWTH Aachen Universität, Aachen, Germany. [2]Jülich Centre for Neutron Science at Heinz Maier-Leibnitz Zentrum, Garching, Germany. [3]Department of Physics "E.R. Caianiello", University of Salerno, Fisciano, Italy. [4]CNR-SPIN c/o University of Salerno, Fisciano, Italy. [5]Neutron Scattering Division, Oak Ridge National Laboratory, Oak Ridge, TN, USA. [6]NIST Center for Neutron Research, National Institute of Standards and Technology, Gaithersburg, MD, USA. [7]Department of Condensed Matter Physics, Faculty of Mathematics and Physics, Charles University, Prague, Czech Republic. [8]Experimental Physics VI, Center for Electronic Correlations and Magnetism, Institute of Physics, University of Augsburg, Augsburg, Germany. [9]Jülich Centre for Neutron Science (JCNS) and Peter Grünberg Institut (PGI), JARA-FIT, Forschungszentrum Jülich, Jülich, Germany. [10]Present address: Department of Materials Science and Engineering, Drexel University, Philadelphia, PA, USA. ✉e-mail: henrik.thoma@frm2.tum.de; rajesh.dutta@frm2.tum.de; vladimir.hutanu@frm2.tum.de

magnetic states, and multiferroic phenomena, have attracted special attention to such materials[12–20]. The quasi 2D characteristic in those compounds is driven by the large cation (e.g., Ba) separating the tetragonal layers hosting the magnetic ion, leading to a significantly stronger symmetric exchange within the layers than between them, as illustrated in Fig. 1[21,22]. Among the Ba-germanates, $Ba_2CoGe_2O_7$ ($S = \frac{3}{2}$) and $Ba_2MnGe_2O_7$ (BMGO, $S = \frac{5}{2}$) exhibit a quasi 2D AFM ordering with magnetic propagation vector $\mathbf{q}_M = (100)$ and $(10\frac{1}{2})$ below $T_N = 6.7$ K and 4.0 K, respectively[22,23]. Their commensurate in-plane AFM moments are favored by the magnetic anisotropy energy (MAE), including the non-vanishing easy-plane single-ion anisotropy (SIA) that gains priority over the weak in-plane component (D_{ab}) of the Dzyaloshinskii–Moriya interaction (DMI) vector, which promotes a spin-spiral structure. Nevertheless, the out-of-plane component of the DMI (D_z) induces a small in-plane canting of the AFM spins, resulting in a weak ferromagnetic (WFM) moment[23,24]. The arrangement of the DMI vector components is illustrated in Fig. 1. The spin-orbit coupling (SOC) and resulting DMI, which are both decisive in the Ba-germanates, have become of particular interest in current condensed matter research as they are present in a wide range of complex magnetic materials. In particular, they are the driving force to stabilize various topological non-collinear magnetic structures like frustrated Heisenberg AFM, spin spirals, magnetic skyrmions, or magnetic soliton lattices[25–29].

A skyrmion phase, which is typically stabilized by DMI in uniaxial non-centrosymmetric antiferromagnets, was predicted in $Ba_2CuGe_2O_7$ (BCGO) by Bogdanov et al. in ref. 30 and immediately after, BCGO became a special candidate in this research field for its incommensurate AFM cycloidal structure with complex magnetic phase diagram under external magnetic fields[31–33]. The Cu^{2+} ion contains only one unpaired 3*d* electron ($S = \frac{1}{2}$) in a d_{xy} orbital in a tetrahedral crystal field, and thus no SIA is expected and the DMI is decisive[21]. The incommensurate AFM spin spiral structure is stabilized below $T_N = 3.26$ K by the competition between the AFM isotropic exchange interaction (J_{ab}) and the in-plane DMI (D_{ab}) for nearest neighbor Cu^{2+} ions[21]. Note that even without SIA, a slight easy-plane MAE is present due to contributions to the Hamiltonian quadratic in D_{ab} that cause odd higher-order Bragg harmonics[34–36]. In addition, an in-plane canting of the AFM spins close to the *ab* plane is favored by the alternating out-of-plane DMI component D_z, inducing a WFM sinusoidal structure perpendicular to the helical plane with the same periodicity as the AFM spin spiral[33].

With regard to frustrated spin structures resulting from competing magnetic interactions, BMGO can not lead to any non-trivial twisted magnetic configuration, e.g., a skyrmion, spin spiral, or soliton phase, as it has a very strong in-plane exchange interaction compared to its DMI and easy-plane type SIA. Interactions that lead to such frustrated phases, mainly found in AFM materials, are the four-spin and frustrated exchange interactions, long-range dipolar interaction, and most importantly the anti-symmetric DMI[26,37,38]. The latter one has a relativistic SOC nature and appears in compounds with locally broken inversion symmetry between the magnetic ions such as for the non-centrosymmetric lattice in BCGO. However, no skyrmion phase could so far be evidenced in BCGO and instead, a helical AFM cycloidal phase is observed at zero field below T_N. Therefore, any indications for frustrated magnetism in the melilite-type compounds remain elusive, and tuning the materials to maximize frustration would be highly desirable, and could be expected in an AFM material showing significant competition between DMI, SIA, and the exchange interactions. Such competitive interactions in the conventional spin Hamiltonian might be realized via doping of the transition metal ion in the host BCGO material. Therefore, $Ba_2Cu_{1-x}Mn_xGe_2O_7$ (BCMGO) could be the ideal choice for the appearance of exotic quantum phenomena resulting from magnetic frustration. Because BCGO can host divalent Mn^{2+} with non-vanishing SIA as a substitution of Cu^{2+} in the range of ($0 \le x \le 1$), one can expect substantial competition between DMI and SIA depending on the doping concentration, possibly enhanced by external magnetic fields. Furthermore, it might provide a deeper insight into the spin-driven multiferroicity, which is attributed to the spin current mechanism for the incommensurate magnetic structure BCGO[3] and to the unconventional *d–p* hybridization mechanism for the commensurate magnetic structure in BMGO[1].

So far, only Granata et al. in ref. 39 reported on the successful synthesis and structural characterization of the polycrystalline BCMGO solid solution series using laboratory X-ray diffraction (XRD). Here, we present a systematic chemical, structural, and magnetic characterization of the polycrystalline BCMGO solid solution series using combined XRD and high-resolution neutron powder diffraction (NPD). It is important to have a precise knowledge of the crystal structure and the magnetic phase diagram to grow high-quality single crystals, to determine the physical properties, and to study the *d–p* hybridization mechanism. It is also a mandatory basis for further theoretical calculations on crystal electric field excitations and the ground states of frustrated magnetism. To develop the rich magnetic phase diagram of BCMGO as a function of the temperature and doping *x*, we have carried out macroscopic heat capacity (HC) and bulk magnetization measurements. We have successfully identified the microscopic orderings in the individual phases using low-temperature NPD, revealing two considerably different magnetic structures below T_N for the Cu-rich compounds with a complex conical AFM phase and the Mn-rich compounds with a 2D-XY AFM structure, separated by a critical phase at $x = 0.57$.

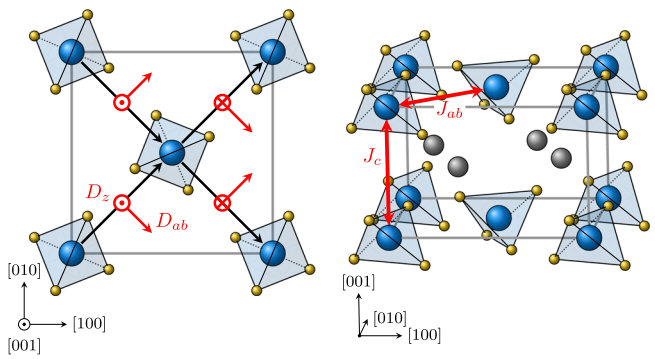

Fig. 1 | Magnetic exchange interactions. Visualization of the potential exchange interactions between nearest neighboring transition metal ions (blue spheres), located in the distorted tetrahedral oxygen environment (yellow spheres) of the $Ba_2TGe_2O_7$ compounds. The magnetic layers (left panel) are separated by large Ba atoms (gray spheres) as shown in the right panel. Non-magnetic Ge_2O_7 structures are removed for clarity. The complete unit cell is displayed in Supplementary Fig. 3. The arrangement of the in-plane (D_{ab}) and out-of-plane (D_z) DMI vector component is displayed for a bonding direction as indicated by the black arrows in the left panel[8]. The intra-plane (J_{ab}) and inter-plane (J_c) symmetric exchange couplings are illustrated by the red arrows in the right panel.

Results

Structural determination of BCMGO using NPD and XRD

The Rietveld structural refinement of the NPD patterns of polycrystalline BCGO ($x = 0$) and BMGO ($x = 1$) collected in the paramagnetic (PM) state at 10 K are shown in Fig. 2a, b, respectively. The calculated intensity (red profile) explains well the majority of the observed peaks with its PM crystal symmetry $P\bar{4}2_1m$; however, there are several clearly evident peaks (marked by black arrows), that are not reproduced. Note that these extra peaks also do not fit into a distorted orthorhombic unit cell. This indicates the presence of at least one other spurious phase, which is typically found in the synthesis, the sample preparation, or the direct sample environment[39]. A selection of possible spurious phases for the $x = 0$ and $x = 1$ compounds and their crystal symmetry is given in Supplementary Tables 1 and 2. By careful inspection, a combination of four different phases, namely $BaCu_2Ge_2O_7$, $Ba_3Ge_3O_9$, $BaCO_3$, and GeO_2 with crystal symmetries *Pnma*, *C*2/*c*, *Pnma*, and $P3_121$, respectively, was successfully identified from a multi-pattern refinement as the best match for the spurious peaks in the $x = 0$ compound. Note that, $Ba_3Ge_3O_9$, $BaCO_3$, GeO_2, and $Ba_2Mn_2Ge_2O_9$ were identified as spurious phases in the $x = 1$ compound, with the latter having a *Pbca* crystal

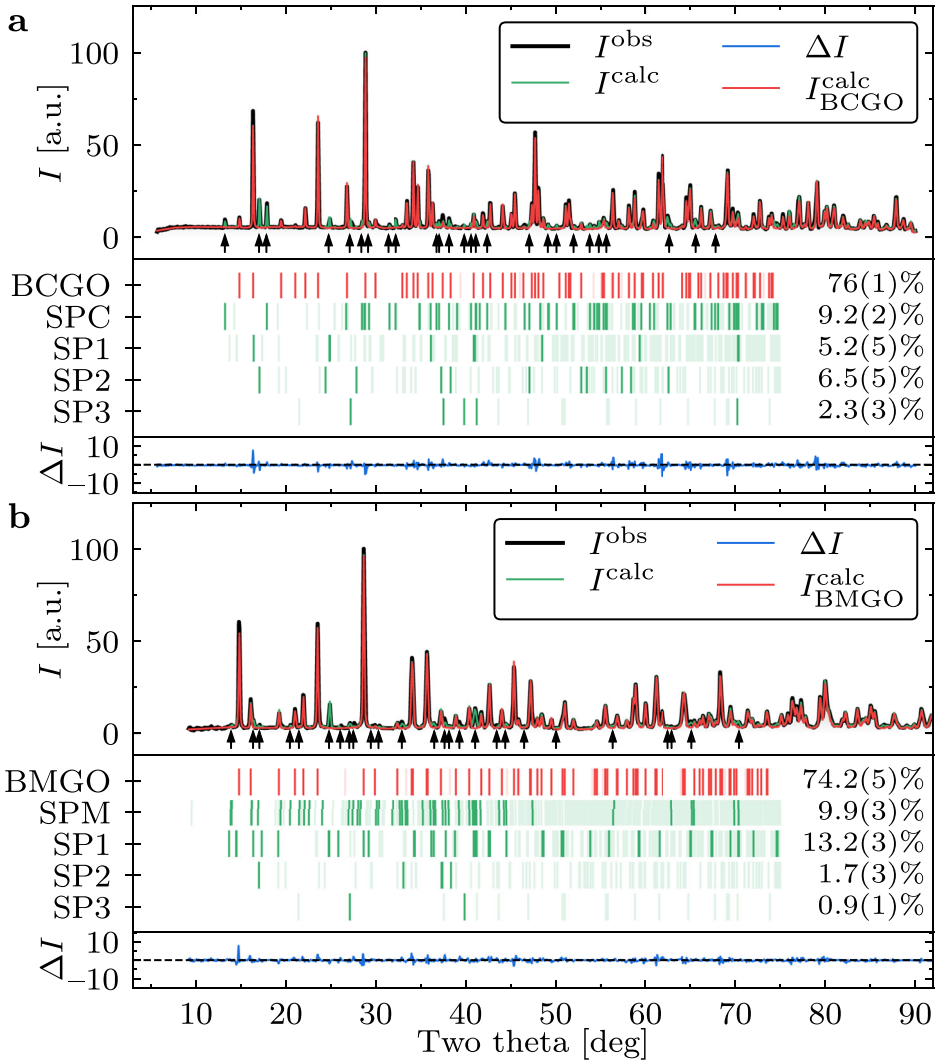

Fig. 2 | PM nuclear structure. The neutron powder diffraction pattern of (**a**) BCGO and **b** BMGO reduced from the time-of-flight measurement at 10 K at POWGEN (SNS) with the center of the wavelength bandwidth at 2.665 Å and 1.5 Å, respectively. Calculated intensity for pure BCGO and BMGO structures are shown in red, whereas the observed intensities are shown in black profile. Non-matching peak positions are marked as black arrows. The fractions of the spurious phases (SPC: $BaCu_2Ge_2O_7$, SPM: $Ba_2Mn_2Ge_2O_9$, SP1: $Ba_3Ge_3O_9$, SP2: $BaCO_3$, and SP3: GeO_2) and their expected peak positions (vertical lines) are given in the central area of each figure. The difference profile between the spurious phases calculated (green line) and observed intensity is shown in blue.

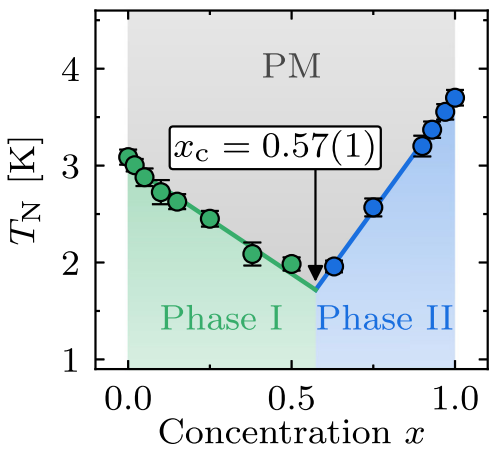

Fig. 3 | Magnetic phase diagram from HC. Dependence of the obtained magnetic phase transition temperatures T_N on x. Details about the determination of T_N can be found in the Supplementary Note 3. The lines are linear fits to the respectively colored symbols that serve as a guide to the eye and define the critical concentration x_c.

symmetry. Taking these additional spurious phases into account, a good match between the calculated (green profile) and observed (black profile) diffraction pattern is achieved. The precise lattice, atomic parameters, and isotropic temperature factors U^{iso} for BCGO and BMGO resulting from the Rietveld refinement of the polycrystalline NPD data collected at 10 K and 100 K, and XRD data at 300 K are listed in Supplementary Tables 3 and 4 and discussed in Supplementary Note 1. The corresponding powder profiles for the 100 K and 300 K refinements for both BCGO and BMGO are shown in Supplementary Figs. 1 and 2, respectively.

As for the $x = 0$ and $x = 1$ end members, some clear spurious peaks were found for almost all samples of the BCMGO solid solution series at room and low temperatures. Selecting the structural parameters of the spurious phases as defined by the multi-pattern refinement for the respective temperatures of 10 K, 100 K, and 300 K, the phase fractions and the BCMGO structure were refined for all measurements of the mixed compounds. An overview of the determined phase fractions for the different samples is given in Supplementary Fig. 3. Nonetheless, precise values for the atomic and lattice parameters of BCMGO could be refined for all temperatures and available concentrations x and are illustrated in Supplementary Fig. 4 and discussed in Supplementary Note 2. In general, a good match between the calculated and observed diffraction patterns could be achieved by Rietveld refinement for all temperatures and mixed

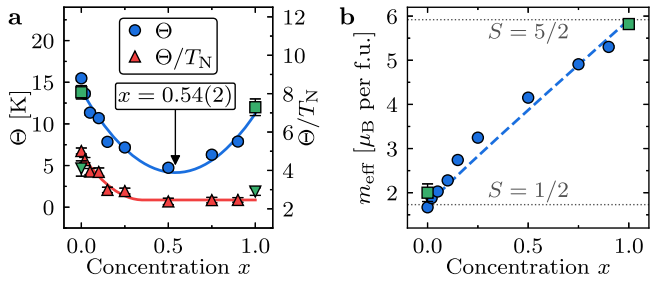

Fig. 4 | CW fits of the magnetization data. CW parameters resulting from the 1 T field-cooled measurements on the polycrystalline BCMGO compounds with different concentrations x. In addition to the absolute CW temperature Θ (blue circles), its ratio to the T_N values from HC measurements is shown in red triangles. The solid blue line is quadratic in x and serves together with the red solid line as a guide to the eye. The m_{eff} values in (**b**) are calculated from the CW constant. The horizontal dotted lines indicate the expected spin-only values for Cu^{2+} ($S = \frac{1}{2}$) and Mn^{2+} ($S = \frac{5}{2}$) and the dashed blue line for their mixture $Cu_{1-x}Mn_x$. The green symbols in (**a**, **b**) correspond to results from single crystals of BCGO ($x = 0$) and BMGO ($x = 1$). Error bars represent one standard deviation.

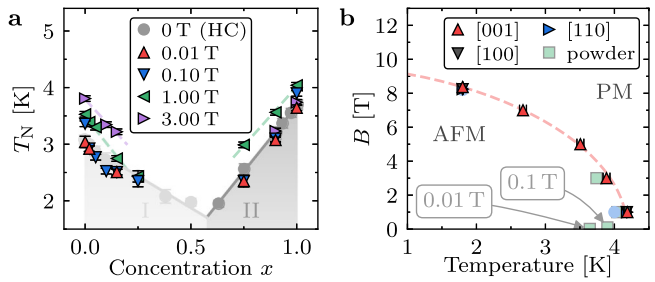

Fig. 5 | Magnetic phase diagram from magnetization data. a Dependence of the obtained magnetic phase transition temperatures T_N on x for the different applied field strengths. The results and the suggested phase boundaries from the HC measurements in Fig. 3b are additionally drawn in light gray. The dashed lines are linear fits to the respective colored symbols and indicate the magnetic field shifted phase boundaries. **b** Magnetic field and temperature-dependent phase diagram in BMGO. The single crystal data points taken from ref. 43 except the green square symbols indicate the results from the BCMGO polycrystalline powder measurements with $x = 1.00$, taken from Fig. 5a. Error bars represent one standard deviation.

compounds. In particular, the high-precision results of the low-temperature NPD measurements at 10 K and 100 K provide an excellent basis for the study of their magnetic properties in the subsequent sections.

Zero-field magnetic phase diagram of BCMGO using HC measurements

The HC of the BCMGO powder samples was measured as a function of temperature from around 1.7 K up to either 20 K (low-temperature region) or 100 K (intermediate temperature range) to determine the magnetic ordering temperature T_N. The detailed procedure is described in Supplementary Note 3 and shown for different compositions in Supplementary Fig. 5. For both Cu- and Mn-rich compounds, a mostly linear decrease of T_N with an increasing mixture is observed and presented in Fig. 3. This effect is maximized at $x = 0.57(1)$ with an expected $T_N \approx 1.7$ K and indicates the presence of two different magnetic phases (Phase I, $x < 0.57$ and Phase II, $x > 0.57$).

In addition to the magnetic phase transition temperature, the HC results in the low-temperature region can be used to quantify the Debye temperature (Θ_D) using a Debye model fit to the data. The obtained Θ_D values are shown in Supplementary Fig. 6b and increase with concentration x as expected by the smaller atomic mass of the Mn compared to the Cu atoms. Note that this Debye contribution at low temperatures accounts only for an effective number of $n_D \approx 3.7$ atoms as demonstrated by an extended Debye–Einstein model fit in Supplementary Note 3 for the four compounds ($x = 0.15$, 0.38, 0.90, and 0.97) measured in the intermediate temperature range. These extended results confirm the presence of phonon modes at higher energies and reproduce well the Θ_D values of the low-temperature fit, demonstrating its reliability.

Magnetic field-dependent magnetic phase diagram of BCMGO using bulk magnetization measurements

Analyzing the 1 T field-cooled magnetization measurements from 300 K to 2 K for the polycrystalline BCMGO compounds, a clearly linear behavior is found in the inverse susceptibility χ_V^{-1} curve above around 50 K, which has an intercept on the negative temperature side as expected for net AFM interactions and can be well described by the Curie–Weiss (CW) law as shown in Supplementary Fig. 7. The absolute CW temperature values (Θ) are presented in Fig. 4a by blue circles. The extracted Θ values are clearly lower for the mixed compounds and the overall behavior can be roughly approximated by a parabola centered at around $x = 0.54(2)$. This resembles the kink in T_N at the critical concentration of $x = 0.57(1)$ in Fig. 3a, separating the two magnetic phases. Note that according to the mean-field theory of a layered AFM, the Θ/T_N ratio is directly connected to the relative size of the inter- and intra-plane exchange constants[40]. Thus, the almost constant Θ/T_N ratios of 2.5(1) for high x values suggest no relative changes in the exchange constants in the framework of the simple AFM model. In contrast, for the low x values, the ratio increases which suggests for the Cu-rich compounds (Phase I) a deviation from the simple AFM model.

The effective magnetic moment (m_{eff}), which is directly connected to the CW constant, is shown in Fig. 4b. Assuming spin-only magnetism, m_{eff} is expected to be 1.73 μ_B and 5.92 μ_B (dotted black lines) for $x = 0.00$ ($S = \frac{1}{2}$) and 1.00 ($S = \frac{5}{2}$), respectively, which provides a good conformity between the expected and measured values for $x = 0.00$. In contrast, m_{eff} is reduced to $S \approx 2.3$ for the $x = 1$ sample due to an admixture of the $Ba_2Mn_2Ge_2O_9$ spurious phase with Mn^{3+} ($S = 2$) ions. Thus, the corresponding distorted data points have been removed from the plot in Fig. 4a,b. However, additional Θ and m_{eff} values for $x = 0$ and 1 (green rectangular symbols) are provided by magnetization measurements on pure single crystals (see Supplementary Fig. 7) for completion. In particular, for BMGO, the values of $\Theta \approx 12$ K and $S \approx 2.45(2)$ confirm this expectation. Considering again spin-only magnetic moments, the expected behavior of m_{eff} for the mixed compounds is depicted by the dashed blue line in Fig. 4b and coincides well with the measurement results for the Cu-rich and Mn-rich compounds. It is interesting to note that only for the mixed compounds between $x = 0.15$ and 0.5, slightly higher values of m_{eff} are measured. Although this difference could, for example, be associated with an incomplete quenching of orbital angular momenta or an increase in the g-factor due to an admixture of exited states by SOC as in the anisotropic g-tensor of single crystalline BCGO[41], these are also likely to result from systematical and experimental inaccuracies. Nevertheless, this peculiar but interesting behavior in the intermediately doped region might be related to the emergence of the conical AFM phase where the incommensurate moment increases with increasing x (see text below).

In addition to the CW parameters, precise T_N values are identified from temperature-dependent magnetization measurements. The detailed procedure is given in Supplementary Note 4 and exemplified for different compositions in Supplementary Fig. 7. In Fig. 5a, the field and x-dependent T_N values are added to the zero-field magnetic phase diagram outlined by HC measurements. As expected, there is a broad consistency between the resulting T_N values for the zero-field HC and the low-field ($B \leq 0.1$ T) magnetization measurements. In contrast, for fields of 1 T, systematically higher T_N values are found for the Cu- and Mn-rich compounds. This magnetic field-induced shift of the phase boundary is depicted by the dashed lines in Fig. 5a. For the Cu-rich compounds, even higher fields of 3 T suggest a further increase in T_N, whereas for the Mn-rich side, T_N reduces again to the low-field value. These results are consistent with the findings in ref. 1, reporting a transition temperature of 4.0 K for applied fields of 1 T in BMGO and temperatures of 3.0 K, 3.3 K, and 3.7 K for fields of 0 T, 1 T, and 3 T in BCGO.

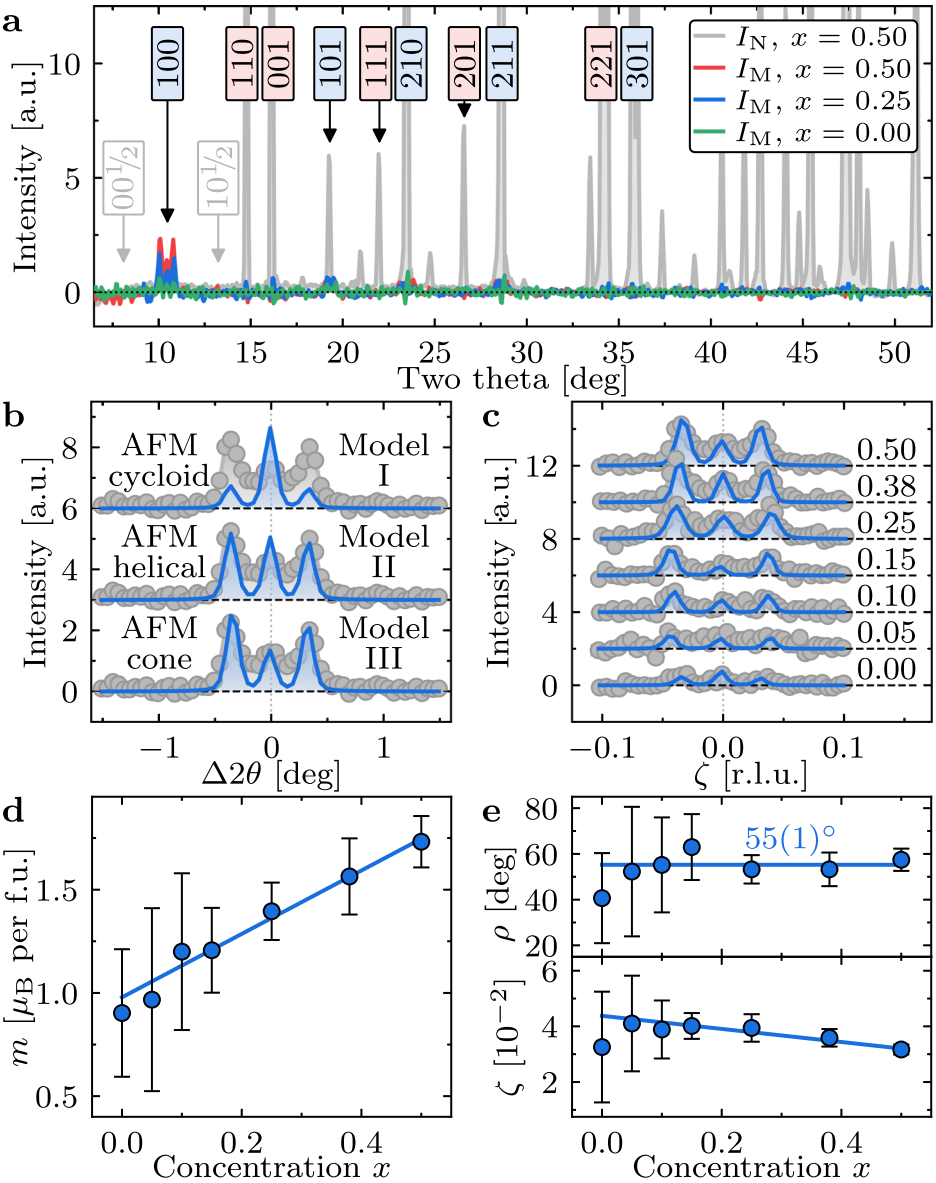

Fig. 6 | Microscopic magnetic structure of Cu-rich compounds. a Magnetic intensity I_M for different Cu-rich BCMGO polycrystalline compounds calculated as the difference between the diffraction patterns measured in the PM and magnetically ordered phase at 10 K and 1.5 K, respectively. Additionally, the PM intensity I_N for the $x = 0.50$ compound at 10 K is shown as a reference. The positions of AFM and FM-type reflections are indicated by blue and red labels, respectively. The gray labels indicate the positions of the first reflection expected for a FM and AFM type ordering with a doubling of the magnetic unit cell in the c direction. The latter corresponds to the magnetic order reported for single crystalline BMGO. **b** Comparison between the observed and refined intensity for the $x = 0.5$ sample with different magnetic models discussed in the text. $\Delta 2\theta$ denotes the difference in two theta to the (100) reflection. **c** Comparison between the observed and refined intensity assuming an AFM cone magnetic model for different concentrations x, labeled on the right side of the figure. The curves in (**b**, **c**) have been shifted vertically by 3 and 2 for clarity, respectively. **d**, **e** Dependence of the total magnetic moment m and half apex angle ρ of the refined AFM cone with incommensurability parameter ζ on the concentration x. The blue solid lines in (**d**, **e**) serve as a guide to the eye and are either linear (**d**, **e** lower panel) or constant (**e** upper panel) fits to the data. Error bars represent one standard deviation.

To complement these studies on the polycrystalline samples, the macroscopic magnetization was also measured on the BCGO and BMGO single crystals, and the parameters are listed in Supplementary Table 7. From the resulting T_N values of the BMGO measurements shown in Fig. 5b, no significant differences are apparent for the three magnetic field directions and a comparably simple phase diagram can be built for BMGO. The T_N values at around 4 K and 1.8 K are reported in ref. 1 for magnetic fields in the [110] direction are shown by light blue circles. The decrease of T_N for $B \geq 1$ T is also reproduced well by the T_N values obtained for the $x = 1.00$ polycrystalline BCMGO powder, taken from Fig. 5a and shown by green squares in Fig. 5b. However, the powder values at 0.01 T and 0.1 T indicate a reduction of T_N also towards low fields for $B < 1$ T, which is not expected for typical AFM systems. This unusual non-monotonic behavior in the AFM phase boundary is similarly found in $Ba_2FeSi_2O_7$ and can be attributed to the quasi-2D character with weak interplane coupling[42].

Zero-field magnetic structure of Cu-rich BCMGO using low-temperature NPD

Additional NPD patterns at 1.5 K were collected for the Cu-rich compounds ($x \leq 0.50$) to microscopically characterize the macroscopically identified Phase I in Fig. 5a. Magnetic structure refinements were conducted systematically based on the low-temperature nuclear structure parameters for the BCMGO compounds determined at 10 K considering all spurious phases previously identified. Magnetic contributions are depicted in Fig. 6a. Two incommensurate satellites accompany the commensurate AFM (100)-type magnetic peaks and these satellites cannot be reasonably indexed by any of the spurious phases identified previously in Supplementary Table 1, confirming their affiliation to the primary BCMGO phase. No magnetic $(10\frac{1}{2})$ peak is evident and thus an AFM type order as found in BMGO can be excluded as well.

Based on the different low-temperature phases reported in BCGO, three potential models can be identified as long-range ordered magnetic structures in the Cu-rich BCMGO compounds. The most obvious choice is certainly a pure AFM cycloidal structure with a cycloidal propagation vector $\boldsymbol{\tau} = (\zeta\zeta 0)$ as reported for low and zero magnetic fields in single crystalline BCGO[31,33]. Note that for each $\boldsymbol{\tau}$ magnetic domains related by a four-fold inversion symmetry are allowed but their magnetic contributions are indistinguishable due to powder averaging. As a result, only contributions at the $(1 \pm \zeta, \pm\zeta, 0)$ satellite positions in the NPD pattern are expected for the AFM cycloidal structure, not at (100). Thus, such a magnetic model can be immediately excluded. In contrast, for an AFM cycloid with $\boldsymbol{\tau} = (\zeta 00)$, denoted as a model I, satellite reflections are expected at the $(1 \pm \zeta, 0, 0)$ and

(1, ζ, 0) positions, with the latter being almost indistinguishable from the (100) peak in the powder profile due to powder averaging. Using this magnetic model, the refinement of the $x = 0.50$ pattern is shown in the upper panel of Fig. 6b. A significantly higher intensity is expected at the central position compared to the satellites at $(1 \pm \zeta, 0, 0)$. This results from the total scattering vector **q** being almost normal to the spin plane for the central (1, ζ, 0) reflection and within the spin plane for the $(1 \pm \zeta, 0, 0)$ satellites. As only the magnetic moments perpendicular to **q** contribute, the magnetic intensities of the satellites are clearly reduced. Therefore, the expected intensity for the pure AFM cycloidal structure does not coincide with the measurement results, and model I can be excluded.

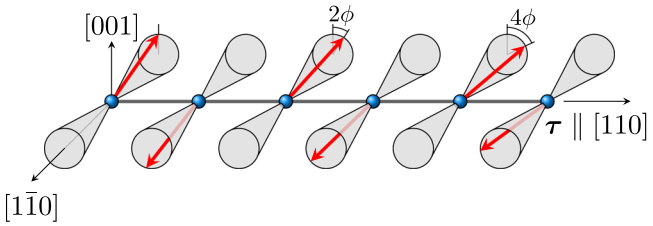

Fig. 7 | Microscopic magnetic structure of $x = 0.5$ phase. The schematic representation of the conical phase (model III) and, constructed using the half apex angle ρ and incommensurability ζ for the phase $x = 0.5$.

To reproduce the intensity of the satellite reflections compared to the central contribution, a helical structure with a spin plane normal to the (ζ00) propagation vector (model II) was assumed. The corresponding refined magnetic intensity for this helical model is shown in the central panel of Fig. 6b. Although it demonstrates a certainly better agreement with the measurement, a lower intensity of the central peak compared to the satellites is clearly evident in the measurement data and cannot be reproduced by the assumed helical magnetic model. Thus, it can also be excluded.

Another model of high magnetic symmetry is the AFM cone structure (model III), which was experimentally evidenced in single crystalline BCGO, though only under applied magnetic fields. It is composed of an AFM cycloidal part with $\boldsymbol{\tau} = (\zeta\zeta 0)$, leading to $(1 \pm \zeta, \zeta, 0)$ type satellite reflections, and a commensurate AFM part with moments in the *ab* plane perpendicular to $\boldsymbol{\tau}$, resulting in a (100) contribution. A refinement of both incommensurate and commensurate magnetic moments results in a good agreement between the observed and calculated intensities as shown in the lower panel of Fig. 6b. The magnetic refinement *R*-factor (2.54%) for model III is significantly improved compared to that (2.64%) for model II. Thus,

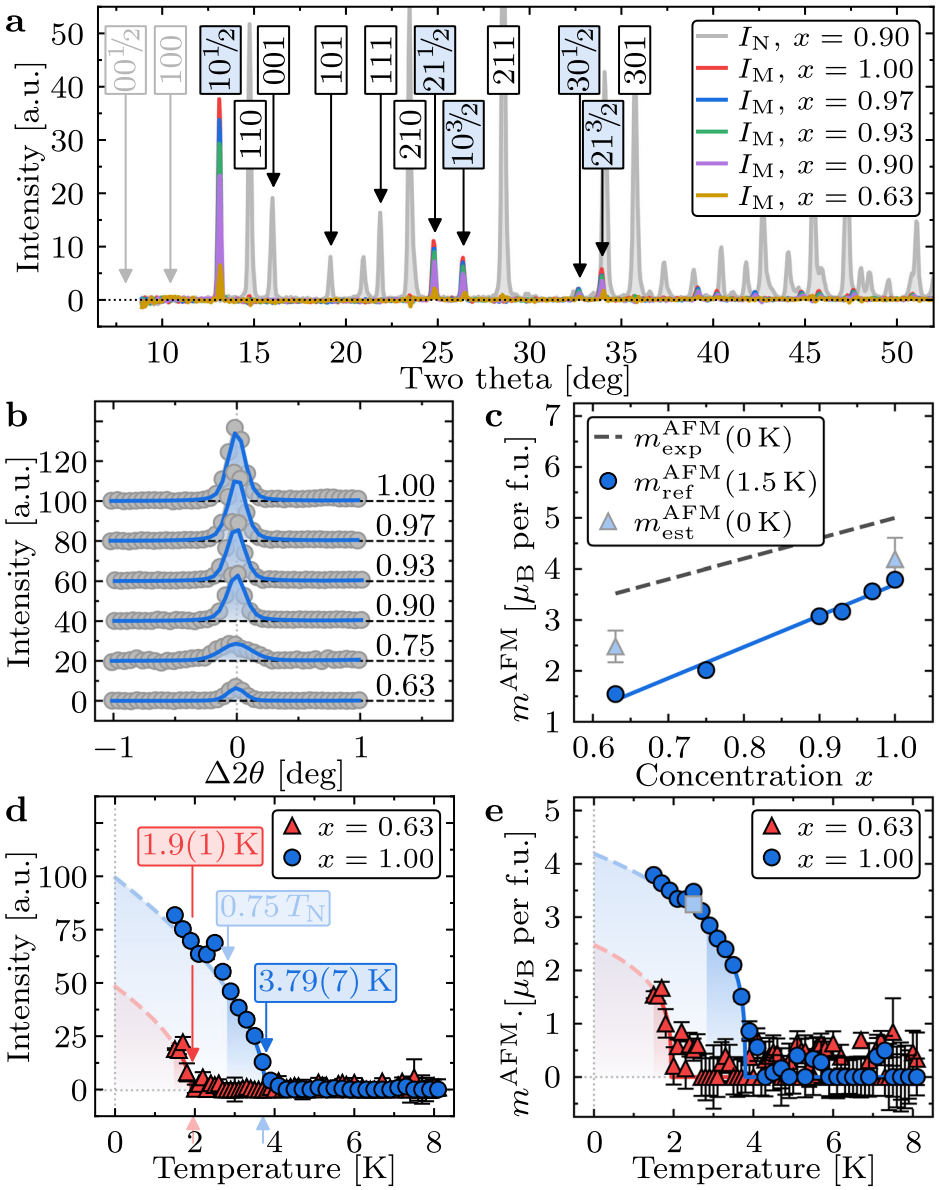

Fig. 8 | Microscopic magnetic structure of Mn-rich compounds. a Magnetic intensity I_M for different Mn-rich BCMGO polycrystalline compounds calculated as the difference between the diffraction patterns measured in the PM and magnetically ordered phase at 10 K and 1.5 K, respectively. Additionally, the PM intensity I_N for the $x = 0.90$ compound at 10 K is shown as a reference. The indices of some magnetic and nuclear reflections are indicated by blue and white labels, respectively. The gray labels indicate the positions of the first reflection expected for an FM and AFM type ordering with and without a doubling of the magnetic unit cell in the *c* direction, respectively. **b** Comparison between the observed and refined magnetic intensity from neutron powder diffraction measurements on BCMGO at 1.5 K assuming an AFM model as discussed in the text. The curves are shifted vertically by 20 for clarity. **c** Dependence of the refined AFM moment at 1.5 K on the concentration *x*. The blue solid line serves as a guide to the eye and is a linear fit to the data. The gray dashed line indicates the $T = 0$ K expectation resulting from the corresponding mixture of Cu^{2+} and Mn^{2+} ions with spin-only moments. **d** Temperature dependence of the intensity for the purely magnetic $(10\frac{1}{2})$ reflection. The blue circles and red triangles indicated the measurement values obtained from neutron powder diffraction on the polycrystalline BCMGO compounds with $x = 1.00$ and 0.63, respectively. The solid lines are critical exponent fits. **e** Estimated temperature dependence of the AFM moment in the two BCMGO compounds, denoted by respective colors and symbols as in (**d**). The estimation is based on the connection $m \propto \sqrt{I_M}$ and scaled by the corresponding AFM moment values for 1.5 K given in Fig. 8c. Error bars represent one standard deviation.

the AFM cone phase can be reliably identified as the high symmetry magnetic structure at zero magnetic fields in Phase I of the mixed BCMGO powder samples. Note that the simultaneous presence of two AFM cycloids with $\boldsymbol{\tau} = (\zeta\zeta 0)$ and $(\zeta 00)$ could also reproduce the measured magnetic intensity but this would correspond to a lower symmetry compared to the proposed AFM cone structure. To completely exclude this possibility, single crystal measurements allowing to distinguish between (1, 0, 0) and (1, ζ, 0) magnetic contributions are required. However, no single crystals are available for the mixed BCMGO compounds yet.

Nevertheless, assuming the AFM cone structure, commensurate and incommensurate AFM moments are refined for all measured Cu-rich mixed BCMGO compounds at 1.5 K. A comparison between the observed and refined intensities close to the magnetic (100) Bragg position is given in Fig. 6c. The magnetic intensity strongly decreases for lower x values, causing an almost linear behavior in the total refined magnetic moment shown in Fig. 6d. The obtained total moment of around 1 μ_B per f.u. for the $x = 0.00$ compound coincides well with spin only moment for Cu^{2+} ions. However, note that the magnetic intensity is only barely visible for the $x \leq 0.10$ compounds in these high-resolution NPD patterns, leading to large uncertainties in the refined values. As a result, a clear distinction between magnetic models cannot be made for small x, in particular for $x = 0.00$ and 0.05. This low magnetic intensity close to the noise level for small concentrations x agrees with the diffraction experiments in ref. 21 that detected hardly any long-range magnetic ordering in BCGO powders. For the half apex angle ρ of the AFM cones, the refinement yields an almost constant value of 55(1)°, displayed in the upper panel of Fig. 6e. In contrast, a slight decrease of the incommensurability parameter ζ for increasing x is visible in the lower panel of Fig. 6e. Nevertheless, the average zeta of around 0.034(1) is close to the value of 0.027 reported for the BCGO single crystals[21,32]. For visualization purposes, we have presented the schematic of the conical magnetic spin structure for model III in Fig. 7. Note that no values for ρ are reported from the single crystalline BCGO measurements in the literature.

Zero-field magnetic structure of Mn-rich BCMGO using low-temperature NPD

Low-temperature NPD at 1.5 K was used to reveal the magnetic ordering for Phase II ($x \geq 0.63$). The intensity difference between the PM (10 K) and the low temperature (1.5 K) NPD profile is shown in Fig. 8a where several sharp peaks with increasing amplitude for higher x values are observed. The peak positions can be unambiguously indexed by a magnetic unit cell doubled in the c direction (see labels in Fig. 8a). Notably, no reasonable indexing of the observed magnetic reflections is possible by any spurious phase identified in Supplementary Table 2, confirming their affiliation to the primary BCMGO phase. Therefore, a doubling of the magnetic unit cell in the c direction as for BMGO can be explicitly identified for the Mn-rich BCMGO compounds. It is noteworthy that the incommensurate peaks from the AFM cone phase in the $x = 0.5$ compound are completely absent already in the $x = 0.63$ compound. Exemplified magnetic structural refinements of the NPD patterns using this commensurate AFM model are shown in Fig. 8b for all measured Mn-rich compounds near the strong $(10\frac{1}{2})$ magnetic Bragg reflection. The refined AFM moments are illustrated in Fig. 8c and show a linear dependence on x. However, they are clearly lower than the expected values illustrated by the dashed line, resulting from the spin-only moments of 1 μ_B and 5 μ_B for Cu^{2+} and Mn^{2+}, respectively. As this difference becomes increasingly larger near smaller x values, this suggests a connection to the linear reduction in T_N towards the equally mixed compounds as evident from HC measurements in Fig. 3a.

The integrated intensity of the $(10\frac{1}{2})$ reflection for the $x = 0.63$ and 1.00 compounds are shown as a function of the temperature in Fig. 8d. The magnetic intensity I_M with decreasing temperature below T_N is typically described close to the magnetic transition by a power law dependence

$$I_M = I_0 \left(\frac{T_N - T}{T_N} \right)^{2\beta} \quad (1)$$

where I_0 is the magnetic intensity at 0 K and β the critical exponent of the magnetic moment $m \propto \sqrt{I_M}$. A corresponding fit to the measured intensities close to the transition temperature with $T/T_N > 0.75$ reveals $T_N = 3.79(4)$ K and $\beta = 0.27(4)$ for $x = 1.00$. This transition temperature is consistent with the value of 3.71(5) determined from HC measurements in Fig. 3a. The small β indicates a two-dimensional AFM characteristic for BMGO, resulting from its layered structure, and is similar to the $\beta = 0.21(4)$ reported for $Ba_2CoGe_2O_7$[4]. Notably, a continuation of the fitted critical exponent curve provides an estimation for the low-temperature values. For the $x = 0.63$ compound, only the onset of the magnetic intensity emerging at low temperatures is probed with a limited number of data points. A refinement of β is not possible and it was thus fixed to the value obtained from the $x = 1.00$ sample and the resulting fit curve is shown as a red line in Fig. 8d. The obtained $T_N = 1.9(1)$ is close to the value of 2.0(1) determined from HC measurements Fig. 3a. In addition, calculated magnetic moments are shown in Fig. 8e. The extrapolation of the exponential fit to those data reveals the AFM moment at 0 K of $m_{est}^{AFM} = 2.5(3)\,\mu_B$ for the $x = 0.63$ and 4.2(4) μ_B for the $x = 1.00$ compound. These 0 K values are indicated in Fig. 8c by triangular symbols. The temperature-dependent results on the $x = 1.00$ compound are additionally supported by neutron diffraction measurements of Sazonov et al. in ref. 43 on the BMGO single crystal. These measurements revealed an AFM moment of around 3.2 μ_B per Mn at 2.5 K, which is consistent with the results on the $x = 1.00$ powder sample as visible in Fig. 8e by the light blue rectangular symbol.

Discussion

The nuclear and magnetic structures of the BCMGO solid solution series in the PM and long-range ordered magnetic phases have been comprehensively studied by macroscopic measurements and high-resolution NPD. Contributions from spurious phases were successfully identified and characterized in a multi-pattern Rietveld refinement. Therefore, precise magnetization and HC quantities were successfully evaluated quantitatively taking into account the impurity phase fractions. Based on the low-temperature HC and magnetization measurements, the magnetic phase diagram of the BCMGO solid solution series and its magnetic field dependence were carefully outlined. This indicates two different ordered magnetic phases for the Cu and Mn-rich sides with transition temperatures between 2 K and 4 K. Applying high-resolution NPD at 1.5 K, an incommensurate AFM cone and a commensurate AFM structure were identified and characterized for the Cu and Mn-rich compounds, respectively. For the latter, the temperature dependence of the magnetic contribution was additionally studied, revealing a reduced critical exponent that suggests a 2D-like behavior as reported, e.g., in $Ba_2CoGe_2O_7$. Note that there is no evidence for a net magnetization complementary to the AFM moments in the macroscopic and diffraction measurements for any concentration x that could hint at a ferrimagnetic behavior, which might arise due to the strong difference of the spin-only magnetic moments of Cu and Mn.

In comparison to these results on BCMGO, magnetization measurements on the $Ba_2Cu_{1-x}Co_xGe_2O_7$ solid solution series reported by Sato et al. in ref. 44 demonstrate the presence of a WFM moment for $x \geq 0.10$%, indicating that already a small Co concentration is sufficient to break the spiral AFM state of BCGO. This is driven by the strong easy-plane type SIA $\gg J \gg D_z$ for the Co ions evidenced in $Ba_2CoGe_2O_7$ by Miyahara and Furukawa in ref. 45. In addition, it is known that pure BCGO single crystals realize a narrow AFM cone phase for applied magnetic fields in the range of $1.95 < B < 2.4$ T in the c direction, contrary to the distorted AFM cycloidal structure at low fields ($B < 1.95$ T)[31–33]. Above 2.4 T, this incommensurate AFM conical phase transitions to a commensurate ordering, where high fields in the [001] direction, which favor an alignment of AFM moments perpendicular to it, act like a strong SIA that forces the structure to be staggered 2D-XY AFM like in $Ba_2CoGe_2O_7$.

In the case of the BCMGO solid solution series, it is fascinating to observe that the AFM cone phase is realized even without a magnetic field and at a very low Mn doping. Although its long-range ordering is less pronounced for $x \leq 0.15$, the satellite signatures are still clearly

visible. However, at higher Mn concentrations, the AFM cone phase is unambiguously evident and its ordered moment gets stronger with increasing $x \geq 0.25$ up to 0.5 (see Fig. 6c), without any staggered AFM signature $(00\frac{1}{2})$, and thus no BMGO phase contamination. This observation closely resembles the case for pure BCGO under an applied field ($1.95 < B < 2.4$ T) along [001] where ζ decreases with the higher field, which is also reflected in Fig. 6e where ζ decreases with higher x. This demonstrates that the induced SIA via the Mn^{2+}-doping acts like an applied magnetic field, which conserves the DMI between the two nearest Cu^{2+} ions, resulting in the formation of the exceptional conical AFM structure. Most interestingly, this AFM cone appears even under zero magnetic field and dominates near $x = 0.5$, which is seemingly a critical phase between the boundary of Phase I and II in Fig. 5a. On the other hand, further doping at $x = 0.63$ completely diminishes the AFM cone structure and transforms it into a 2D-XY AFM alignment with continuously increasing moments until $x = 1$. This behavior can be related to the incommensurate to commensurate transition in pure BCGO, such that the Mn-induced SIA for $x \geq 0.63$ in BCMGO acts like an effective magnetic field with $B > 2.4$ T in the [001] direction.

This dependency of the AFM cone shows again the importance of the emerging SIA connected to the Mn doping. It is important to emphasize that SIA-driven effective fields have not only a doping-dependent strength but also a well-defined crystal direction. This might be particularly valuable for powder samples, for which the application of external magnetic fields in only a certain lattice direction is not possible. Single crystals benefit from the induced effective field as they intrinsically have a perfect alignment and a static nature. Thus, replacing an external field with a static SIA-driven effective one through dedicated doping may open up new perspectives and capabilities in designing, modeling, and tuning compounds with a set of desired interactions and magnetic properties.

Based on these findings and the significant doping-dependent differences in the realized magnetic structures, it became clear how these differently signed and sized coupling effects compete in the mixed compounds of the BCMGO solid solution series, providing valuable insight in the fundamentals of their magnetic ordering. To summarize, all these observations reinforce the conclusion that the conical AFM structure in BCMGO most likely results from the delicate balance between the competing interactions of the transition metal ions, namely symmetric exchange, SIA, and DMI. In addition, the provided detailed information about the nuclear and magnetic structures of the BCMGO solid solution series will serve as a valuable reference for further experimental and theoretical studies based on single crystals. In particular, the presence of the strong AFM cone structure in the mixed BCMGO compound with $x = 0.50$ provides promising characteristics towards exciting magnetic structures of a complex twisted type like the stable skyrmion phase suggested for BCGO in ref. 30. Clearly, in-depth studies focusing on the here identified critical region $0.5 < x < 0.63$ will be of high interest.

Methods

Polycrystalline sample preparation

$Ba_2Cu_{1-x}Mn_xGe_2O_7$ powders have been synthesized as pressed pellets in the Department of Physics, University of Salerno, Italy, using a dedicated heating procedure, and the morphology and chemical composition were characterized by scanning electron microscopy (SEM) and energy dispersive spectroscopy (EDS), as described in detail in ref. 39. By adjusting the stoichiometric ratio of the starting materials and optimizing the synthesis procedure, it could provide polycrystalline samples with $x = 0.00, 0.01, 0.02, 0.05, 0.10, 0.15, 0.25, 0.38, 0.50, 0.63, 0.75, 0.90, 0.93, 0.97$, and 1.00. For each composition, a pellet with a mass of up to 15 g was synthesized. For the magnetization and diffraction measurements, a portion of the raw pellets was ground using an agate mortar and pestle. In particular, for neutron and X-ray powder diffraction, extensive and careful grinding is essential to avoid texture effects. In addition, some of the $Ba_2Cu_{1-x}Mn_xGe_2O_7$ powder was pressed into thin plates for HC measurements using a manual press with a 3 mm and 6 mm pressing die. By manually cutting the plates, samples with various diameters were prepared, where the typical weight of a 3 mm diameter plate was around 5 mg.

BCGO and BMGO single crystals

High-quality BCGO and BMGO single crystals were grown by the floating zone technique at the Department of Physics, University of Salerno, Italy. Details about the growing process and their characterization are given in refs. 46,47.

Powder diffraction and macroscopic measurements

Room temperature X-ray and low-temperature neutron powder diffraction measurements were performed on the BCMGO polycrystalline powders using the laboratory X-ray diffractometer Bruker D2 PHASER at the outstation of the Jülich Center for Neutron Science (JCNS) in Garching, Germany, and the time-of-flight (TOF) neutron powder diffractometer POWGEN[48] at the Spallation Neutron Source (SNS) of the Oak Ridge National Laboratory (ORNL) in Oak Ridge, Tennessee, United States, respectively. Additional diffraction measurements were performed at the BT-1 high-resolution neutron powder diffractometer at the NIST Center for Neutron Research in Gaithersburg, Maryland, United States. For the NPD at POWGEN, around 5 g of BCMGO powder was filled in a 8 mm vanadium can and mounted in an orange-type cryostat, which can reach sample temperatures of around 1.5 K. For the experiment, the instrument was driven in high-resolution mode with the center of the bandwidth chopper either at a wavelength of 1.500 Å or 2.665 Å. For the experiment at BT-1, the sample was similarly prepared and measured with a monochromatic neutron wavelength of 1.54 Å in steps of 0.05° in two theta, in a cryostat with a base temperature of 300 mK. All powder diffraction patterns were refined using the JANA2006 software[49,50], considering the powder averaging of both the nuclear and magnetic structure. The HC and magnetization measurements were carried out using the commercially available Quantum Design physical property measurement system Dynacool at the JCNS in Jülich, Germany. Complementary HC measurements were performed at the Physics Department of the University of Augsburg, Germany, and the Material Growth & Measurement Laboratory in Prague, Czech Republic.

TOF data analysis

Using the Mantid software, the TOF data, collected with a 2D detector, was automatically combined, integrated, and reduced as described in detail in ref. 48. For the usage in the refinement software, the d-spacing of the resulting diffraction pattern was converted into two theta values, assuming a wavelength of 1.54 Å and performing a third-order spline interpolation in angular steps of 0.05° by the interp1d function of the SciPy package[51].

Data availability

All data supporting the findings of this study are available from the corresponding authors upon reasonable request.

Received: 20 January 2024; Accepted: 10 July 2024;
Published online: 29 July 2024

References

1. Murakawa, H., Onose, Y., Miyahara, S., Furukawa, N. & Tokura, Y. Comprehensive study of the ferroelectricity induced by the spin-dependent d–p hybridization mechanism in $Ba_2XGe_2O_7$ (X = Mn, Co, and Cu). *Phys. Rev. B* **85**, 174106 (2012).
2. Murakawa, H., Onose, Y., Miyahara, S., Furukawa, N. & Tokura, Y. Ferroelectricity induced by spin-dependent metal-ligand hybridization in $Ba_2CoGe_2O_7$. *Phys. Rev. Lett.* **105**, 137202 (2010).
3. Murakawa, H., Onose, Y. & Tokura, Y. Electric-field switching of a magnetic propagation vector in a helimagnet. *Phys. Rev. Lett.* **103**, 147201 (2009).

4. Hutanu, V. et al. Evolution of two-dimensional antiferromagnetism with temperature and magnetic field in multiferroic $Ba_2CoGe_2O_7$. *Phys. Rev. B* **89**, 064403 (2014).
5. Hutanu, V. et al. Determination of the magnetic order and the crystal symmetry in the multiferroic ground state of $Ba_2CoGe_2O_7$. *Phys. Rev. B* **86**, 104401 (2012).
6. Sazonov, A. et al. Crystal structure of magnetoelectric $Ba_2MnGe_2O_7$ at room and low temperatures by neutron diffraction. *Inorg. Chem.* **57**, 5089 (2018).
7. Dutta, R. et al. Topological analysis of the experimental electron density in multiferroic antiferromagnet $Ba_2MnGe_2O_7$. *IEEE Trans. Magn.* **58**, 2500206 (2022).
8. Thoma, H. et al. Magnetic order and sign of the Dzyaloshinskii–Moriya interaction in 2-D antiferromagnet $Ba_2CoGe_2O_7$ under applied magnetic field. *IEEE Trans. Magn.* **58**, 6400305 (2022).
9. Romhányi, J., Pollmann, F. & Penc, K. Supersolid phase and magnetization plateaus observed in the anisotropic spin-$\frac{3}{2}$ Heisenberg model on bipartite lattices. Phys. Rev. B 84, 184427 (2011)..
10. Weihong, Z., McKenzie, R. H. & Singh, R. R. P. Phase diagram for a class of spin-$\frac{1}{2}$ Heisenberg models interpolating between the square-lattice, the triangular-lattice, and the linear-chain limits. Phys. Rev. B 59, 14367 (1999)..
11. Chakravarty, S., Halperin, B. I. & Nelson, D. R. Two-dimensional quantum Heisenberg antiferromagnet at low temperatures. *Phys. Rev. B* **39**, 2344 (1989).
12. Dutta, R. et al. Spin dynamics study and experimental realization of tunable single-ion anisotropy in multiferroic $Ba_2CoGe_2O_7$ under external magnetic fields. *Phys. Rev. B* **104**, L020403 (2021).
13. Soda, M. et al. Spin-nematic interaction in the multiferroic compound $Ba_2CoGe_2O_7$. *Phys. Rev. Lett.* **112**, 127205 (2014).
14. Penc, K. et al. Spin-stretching modes in anisotropic magnets: spin-wave excitations in the multiferroic $Ba_2CoGe_2O_7$. *Phys. Rev. Lett.* **108**, 257203 (2012).
15. Bordács, S. et al. Chirality of matter shows up via spin excitations. *Nat. Phys.* **8**, 734 (2012).
16. Hasegawa, S. et al. Nontrivial temperature dependence of magnetic anisotropy in multiferroic $Ba_2MnGe_2O_7$. *Phys. Rev. Res.* **3**, L032023 (2021).
17. Kézsmárki, I. et al. One-way transparency of four-coloured spin-wave excitations in multiferroic materials. *Nat. Commun.* **5**, 3203 (2014).
18. Do, S.-H. et al. Understanding temperature-dependent SU(3) spin dynamics in the $S = 1$ antiferromagnet $Ba_2FeSi_2O_7$. *npj Quantum Mater.* **8**, 5 (2023).
19. Do, S. H. et al. Decay and renormalization of a longitudinal mode in a quasi-two-dimensional antiferromagnet. *Nat. Commun.* **12**, 5331 (2021).
20. Watanabe, Y. et al. Double dome structure of the Bose–Einstein condensation in diluted $S = 3/2$ quantum magnets. *Nat. Commun.* **14**, 1260 (2023).
21. Zheludev, A., Shirane, G., Sasago, Y., Kiode, N. & Uchinokura, K. Spiral phase and spin waves in the quasi-two-dimensional antiferromagnet $Ba_2CuGe_2O_7$. *Phys. Rev. B* **54**, 15163 (1996).
22. Masuda, T. et al. Instability of magnons in two-dimensional antiferromagnets at high magnetic fields. *Phys. Rev. B* **81**, 100402 (2010).
23. Zheludev, A. et al. Spin waves and the origin of commensurate magnetism in $Ba_2CoGe_2O_7$. *Phys. Rev. B* **68**, 024428 (2003).
24. Endo, T., Doi, Y., Hinatsu, Y. & Ohoyama, K. Magnetic and neutron diffraction study on melilite-type oxides $Sr_2MGe_2O_7$ (M = Mn, Co). *Inorg. Chem.* **51**, 3572 (2012).
25. Bode, M. et al. Chiral magnetic order at surfaces driven by inversion asymmetry. *Nature* **447**, 190 (2007).
26. Heinze, S. et al. Spontaneous atomic-scale magnetic skyrmion lattice in two dimensions. *Nat. Phys.* **7**, 713 (2011).
27. Togawa, Y. et al. Chiral magnetic soliton lattice on a chiral helimagnet. *Phys. Rev. Lett.* **108**, 107202 (2012).
28. Zhang, S. et al. Giant Dzyaloshinskii–Moriya interaction, strong XXZ-type biquadratic coupling, and bimeronic excitations in the two-dimensional $CrMnI_6$ magnet. *npj Quantum Mater.* **8**, 38 (2023).
29. Barts, E. & Mostovoy, M. Magnetic particles and strings in iron langasite. *npj Quantum Mater.* **6**, 104 (2021).
30. Bogdanov, A. N., Rößler, U. K., Wolf, M. & Müller, K.-H. Magnetic structures and reorientation transitions in noncentrosymmetric uniaxial antiferromagnets. *Phys. Rev. B* **66**, 214410 (2002).
31. Mühlbauer, S., Gvasaliya, S. N., Pomjakushina, E. & Zheludev, A. Double-*k* phase of the Dzyaloshinskii–Moriya helimagnet $Ba_2CuGe_2O_7$. *Phys. Rev. B* **84**, 180406(R) (2011).
32. Mühlbauer, S., Gvasaliya, S., Pomjakushina, E. & Zheludev, A. Phase diagram of the Dzyaloshinskii–Moriya helimagnet $Ba_2CuGe_2O_7$ in canted magnetic fields. *Phys. Rev. B* **86**, 024417 (2012).
33. Mühlbauer, S., Brandl, G., Månsson, M. & Garst, M. Formation of incommensurate long-range magnetic order in the Dzyaloshinskii–Moriya antiferromagnet $Ba_2CuGe_2O_7$ studied by neutron diffraction. *Phys. Rev. B* **96**, 134409 (2017).
34. Kaplan, T. A. Single-band Hubbard model with spin-orbit coupling. *Z. Phys. B* **49**, 313 (1983).
35. Shekhtman, L., Entin-Wohlman, O. & Aharony, A. Moriya's anisotropic superexchange interaction, frustration, and Dzyaloshinsky's weak ferromagnetism. *Phys. Rev. Lett.* **69**, 836 (1992).
36. Zheludev, A. et al. Magnetic anisotropy and low-energy spin waves in the Dzyaloshinskii–Moriya spiral magnet $Ba_2CuGe_2O_7$. *Phys. Rev. B* **59**, 11432 (1999).
37. Okubo, T., Chung, S. & Kawamura, H. Multiple-*q* states and the Skyrmion lattice of the triangular-lattice Heisenberg antiferromagnet under magnetic fields. *Phys. Rev. Lett.* **108**, 017206 (2012).
38. Bogdanov, A. & Hubert, A. Thermodynamically stable magnetic vortex states in magnetic crystals. *J. Magn. Magn. Mater.* **138**, 255 (1994).
39. Granata, V. et al. Synthesis and characterization of mixed melilite-type oxides. *J. Cryst. Growth* **457**, 128 (2017).
40. Gross, R. & Marx, A. *Festkörperphysik*, 2nd edn, 727–730 (De Gruyter Oldenbourg, 2014) https://doi.org/10.1524/9783110358704.
41. Zheludev, A., Maslov, S. & Shirane, G. Field-induced incommensurate-to-commensurate transition in $Ba_2CuGe_2O_7$. *Phys. Rev. B* **57**, 2968 (1998).
42. Jang, T.-h et al. Physical properties of the quasi-two-dimensional square lattice antiferromagnet $Ba_2FeSi_2O_7$. *Phys. Rev. B* **104**, 214434 (2021).
43. Sazonov, A. et al. Magnetic structure of the magnetoelectric material $Ba_2MnGe_2O_7$. *Phys. Rev. B* **108**, 094412 (2023).
44. Sato, T., Masuda, T. & Uchinokura, K. Magnetic property of $Ba_2CoGe_2O_7$. *Phys. B Condens. Mater.* **329–333**, 880–881 (2003).
45. Miyahara, S. & Furukawa, N. Theory of magnetoelectric resonance in two-dimensional S=$\frac{3}{2}$ antiferromagnet $Ba_2CoGe_2O_7$ via spin-dependent metal-ligand hybridization mechanism. J. Phys. Soc. Jpn. 80, 073708 (2011)..
46. Fittipaldi, R. et al. Crystal growth and characterization of the non-centrosymmetric antiferromagnet $Ba_2CuGe_2O_7$. *J. Cryst. Growth* **404**, 223 (2014).
47. Granata, V. et al. Effect of different atmospheres on the synthesis of $Ba_2CuGe_2O_7$ single crystals. *Eur. Phys. J. Spec. Top.* **228**, 703 (2019).
48. Huq, A. et al. POWGEN: rebuild of a third-generation powder diffractometer at the spallation neutron source. *J. Appl. Cryst.* **52**, 1189 (2019).
49. Petříček, V., Dušek, M. & Palatinus, L. Crystallographic computing system JANA2006: general features. *Z. Kristallogr. Cryst. Mater.* **229**, 345 (2014).
50. Petříček, V., Henriques, M. S. & Dušek, M. Solution and refinement of magnetic structures with Jana 2006. *Acta Phys. Pol. A* **130**, 848 (2016).

51. Virtanen, P. et al. SciPy 1.0: fundamental algorithms for scientific computing in Python. *Nat. Methods* **17**, 261 (2020).

Acknowledgements
Specific heat measurements were performed in MGML (mgml.eu), which is supported within the program of Czech Research Infrastructures (project no. LM2023065). A portion of this research used resources at the SNS, a DOE Office of Science User Facility operated by the ORNL. The identification of any commercial product or trade name does not imply endorsement or recommendation by the National Institute of Standards and Technology.

Author contributions
M.A. and V.H. conceived and supervised the project. The HC measurements were carried out by P.Č., N.K., and H.T. The magnetic susceptibility measurements were conducted by H.T. in discussion with S.N. The neutron powder diffraction experiments were performed by H.T. and V.H., supported by Q.Z. at POWGEN (SNS) and by J.L. at BT-1 (NIST). H.T. V.H., M.A., and R.D. contributed to the analysis and interpretation of the data. The single- and polycrystalline samples have been grown by V.G., supervised by R.F., and prepared for the measurements by H.T. The paper is written by R.D. and H.T. and all co-authors made comments on the paper.

Funding
Open Access funding enabled and organized by Projekt DEAL.

Competing interests
The authors declare no competing interests.

Additional information
Supplementary information The online version contains supplementary material available at https://doi.org/10.1038/s41535-024-00665-z.

Correspondence and requests for materials should be addressed to Henrik Thoma, Rajesh Dutta or Vladimir Hutanu.